JOURNAL OF APPLIED CRYSTALLOGRAPHY
ISSN 1600-5767

Three-dimensional grain resolved strain mapping using laboratory X-ray diffraction contrast tomography: theoretical analysis

Adam Lindkvist* and Yubin Zhang

Department of Mechanical Engineering, Technical University of Denmark, Kongens Lyngby 2800, Denmark.
*Correspondence e-mail: adli@mek.dtu.dk

Received 23 May 2021
Accepted 26 October 2021

Edited by A. Borbély, Ecole National Supérieure des Mines, Saint-Etienne, France

Keywords: strain; stress; laboratory diffraction contrast tomography (LabDCT); three-dimensional mapping; laboratory X-ray strain mapping (LabXRS).

Laboratory diffraction contrast tomography (LabDCT) is a recently developed technique to map crystallographic orientations of polycrystalline samples in three dimensions non-destructively using a laboratory X-ray source. In this work, a new theoretical procedure, named LabXRS, expanding LabDCT to include mapping of the deviatoric strain tensors on the grain scale, is proposed and validated using simulated data. For the validation, the geometries investigated include a typical near-field LabDCT setup utilizing Laue focusing with equal source-to-sample and sample-to-detector distances of 14 mm, a magnified setup where the sample-to-detector distance is increased to 200 mm, a far-field Laue focusing setup where the source-to-sample distance is also increased to 200 mm, and a near-field setup with a source-to-sample distance of 200 mm. The strain resolution is found to be in the range of 1–5 $\times 10^{-4}$, depending on the geometry of the experiment. The effects of other experimental parameters, including pixel binning, number of projections and imaging noise, as well as microstructural parameters, including grain position, grain size and grain orientation, on the strain resolution are examined. The dependencies of these parameters, as well as the implications for practical experiments, are discussed.

1. Introduction

Most engineering materials are polycrystalline and have local elastic anisotropy. This means that complex heterogeneous stress states are present, even in single-phase materials that are deformed uniaxially due to differences in crystallographic orientation (Bhattacharyya *et al.*, 2020; Oddershede *et al.*, 2010). The stress state is further complicated by plastic deformation (Levine *et al.*, 2011), as well as by the presence of multiple phases (Zhang *et al.*, 2019). The evolution of the microscopic stress state of a polycrystalline material under any load is of significant interest since it is a crucial part of any model capable of accurately predicting the mechanical behavior and failure mechanisms of a material. However, one of the major hurdles of developing such a model is the difficulty of non-destructively measuring the local stress states. Only during the past two decades have several methods enabling these kinds of measurements been developed, including 3D X-ray diffraction (3DXRD) (Jensen & Poulsen, 2012; Margulies *et al.*, 2001; Poulsen *et al.*, 2001), X-ray Laue microdiffraction (Larson *et al.*, 2002; Larson & Levine, 2013; Zhang & Barabash, 2019) and dark-field X-ray microscopy (Poulsen *et al.*, 2018; Simons *et al.*, 2015, 2018). Further specialization of the 3DXRD technique to improve the conditions for strain measurements has resulted in high-energy diffraction microscopy (HEDM) and high-resolution

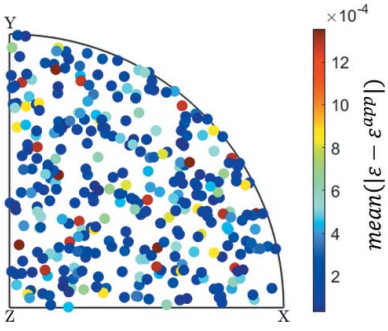

reciprocal-space mapping, as well as scanning 3DXRD (Bernier *et al.*, 2011; Hayashi *et al.*, 2015; Jakobsen *et al.*, 2006). Due to the high resolution and flexibility of these techniques, local strain measurements have almost become synonymous with synchrotron X-rays. This means, however, that the number of experiments is severely limited by the scarcity of synchrotron facilities. Development of a laboratory technique would not only increase the rate at which these experiments can be performed but also encourage much more industrial involvement.

Laboratory X-ray diffraction contrast tomography (LabDCT) is an emerging technique used for non-destructive characterization of crystallographic orientations of individual grains in three dimensions (Bachmann *et al.*, 2019; King *et al.*, 2013, 2014). It has many things in common with its synchrotron variant, diffraction contrast tomography (DCT) (Ludwig *et al.*, 2008; Reischig *et al.*, 2013), which is a special case of the 3DXRD technique. However, what sets it apart is that it uses divergent polychromatic X-rays from a laboratory X-ray tube (King *et al.*, 2013; McDonald *et al.*, 2015), rather than parallel monochromatic synchrotron X-rays. The polychromatic (or 'white') beam is what enables the use of low-flux laboratory sources without requiring a proportional increase in experimental time. The LabDCT technique has been shown to produce grain maps with a spatial resolution of ∼5–10 µm and an orientation resolution of 0.1° (McDonald *et al.*, 2017, 2021; Oddershede *et al.*, 2019; Sun *et al.*, 2017, 2019).

Given the general similarities and the comparable orientation resolution, which has been reported to be in the range of 0.05–0.1° for synchrotron DCT (Ludwig *et al.*, 2008; Menasche *et al.*, 2020), it is reasonable to assume that it should be possible to retrieve strain information along with the orientation of each grain using LabDCT, much like 3DXRD (Bernier *et al.*, 2011; Hall *et al.*, 2018; Oddershede *et al.*, 2010, 2011), as well as DCT (Reischig *et al.*, 2013). However, the polychromatic beam used in LabDCT results in the Bragg condition being fulfilled for many grains and (*hkl*) planes at once, without needing to rock the sample. As a result, the dilatational strain, *i.e.* the change of unit-cell volume, is not directly accessible (Chung & Ice, 1999). However, since the deviatoric strain changes the direction of the diffraction vector, rather than just the length, it is possible to evaluate the deviatoric strain using a white beam.

Another important lesson that can be learned from 3DXRD is related to the tuning of the distance between the sample and the detector. Experiments using shorter distances (*i.e.* 10 mm or less), such as DCT, are commonly referred to as near-field experiments and place an emphasis on real-space resolution. Far-field experiments, on the other hand, have sample-to-detector distances of anything from centimetres to metres. This is done to increase the reciprocal-space resolution, including the strain resolution, which can approach 10^{-5} for the most extreme far-field cases (Miller *et al.*, 2020) while the strain resolution of synchrotron DCT is limited to a few times 10^{-4} (Reischig *et al.*, 2013). The applicability of this 'lesson' to the case of LabDCT needs to be examined. In addition, the effects of the source-to-sample distance also need investigation, since the conical beam is likely to make this an important parameter, unlike in the synchrotron case.

The aim of the present work is to introduce a novel theoretical procedure, which has been named laboratory X-ray strain mapping (LabXRS), that can be used to map the deviatoric strain on the grain scale using data from a LabDCT experiment. LabXRS will allow access to local strain mapping for those that do not have easy access to an adequate synchrotron source. LabXRS will be described in detail in Section 2, with emphasis on the general concepts that are independent of both the experimental parameters and the data analysis. This will be followed by an example of a way to implement LabXRS using forward simulations in Section 3. In Section 4, the effects of several LabDCT experimental setup parameters on the strain resolution are presented on the basis of simulated diffraction data, where ground-truth strain components are known. Finally, possible mechanisms behind any observed errors are discussed in Section 5.

2. Theoretical procedure

The geometrical setup of LabDCT is shown in Fig. 1. The sample is placed between the source and the 2D detector, at fixed distances L_{ss} and L_{sd}. For LabDCT measurements using the Zeiss Xradia Versa series commercial X-ray microscopes, these distances are typically in the 11–15 mm range. When $L_{ss} = L_{sd}$, an effect known as Laue focusing occurs, focusing diffracting X-rays of different wavelengths in the direction normal to the diffracting plane. If L_{sd} is greater than L_{ss}, the spots will instead be magnified, as well as inverted, in this direction. The spots will be magnified in proportion to L_{sd} in all other directions. The magnification is reduced with increasing L_{ss} due to the beam approaching parallelity. If L_{ss} is

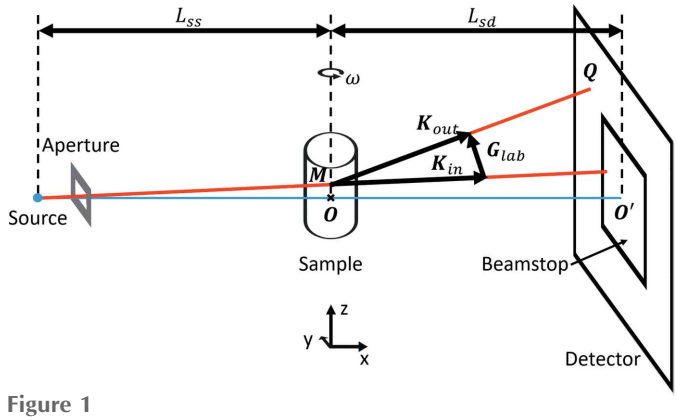

Figure 1
A schematic of a typical LabDCT setup with one diffracted and one transmitted X-ray beam highlighted. The conical beam is confined by an aperture to avoid illumination of the whole detector with the direct beam. Some of the X-rays of a specific wavelength passing through the point **M** (x_m, y_m, z_m) in the sample diffract, producing a spot on the detector at **Q** (L_{sd}, y_{det}, z_{det}). The laboratory coordinate system is defined with the intersection between the beam center and the sample rotational axis, **O**, as the origin. The **x** direction is defined as being parallel to the beam, the **z** direction as parallel to the sample rotation axis and the **y** direction as the cross product of these. The distance between the source and the sample, L_{ss}, is not necessarily equal to the distance between the sample and the detector, L_{sd}, although it is the most common setup.

larger than L_{sd}, lesser focusing along the diffraction vector will occur, resulting in spots approaching an orthographic projection of the grains with increasing L_{ss}.

The polychromatic beam is confined by an aperture to limit the angular coverage to the minimum required to illuminate the sample (see Fig. 1). The region of the detector within the angular coverage of the direct beam is shielded by a beam stop. A portion of the X-rays passing through the sample will diffract, producing spots of high intensity on the detector. The sample is then rotated 360° about the z axis with fixed intervals. The resulting data set consists of intensities in every pixel on the detector, *i.e.* a greyscale image commonly referred to as a projection, for each rotational angle ω. These projections can then be reconstructed into a 3D orientation map of the grain structure, provided that the grains are sufficiently large (typically >20 µm) and have low enough internal misorientation. A commonly used algorithm for this reconstruction is the forward-simulation-based fast geometric indexing algorithm implemented in the commercial software *Grainmapper3D* (Bachmann *et al.*, 2019).

The algebra for relating the observed diffraction patterns to information on the unit cell in reciprocal space necessitates the introduction of a set of coordinate systems. The first is the laboratory coordinate system, which is related to the positions of the rotation axis, source and detector (see Fig. 1). The next is the rotated coordinate system, which is identical to the laboratory system except that it is rotated along with the sample according to the angle ω. In materials science, it is common to use reference directions such as the rolling direction to define the sample system. Finally, a Cartesian grain system is defined for each grain, with axes parallel to the lattice vectors (commonly denoted by **a**, **b**, **c**). To help distinguish between these coordinate systems, the axes of the laboratory system will be referred to as x, y, z and the axes of the Cartesian grain system will be numbered. For instance, $\varepsilon_{x,x}$ is the normal strain component along the x axis, while $\varepsilon_{1,1}$ is the normal strain component along [100] of the individual grain.

As long as the setup geometry, the diffracting lattice plane (*hkl*), strain and orientation of a grain are known, the diffraction vector, $\mathbf{G}_{lab}$, can be determined using forward-simulation models [see *e.g.* Fang *et al.* (2020)]. When the sample is elastically strained, the grain lattice distorts, leading to changes in the diffraction vectors for each diffraction event. $\mathbf{G}_{lab}$ for lattice plane (*hkl*) can then be determined as (Poulsen, 2004; Poulsen *et al.*, 2001)

$$\mathbf{G}_{lab} = \mathbf{\Omega T g}^{-1}\mathbf{B}_0(\mathbf{I}+\varepsilon)^{-1}\mathbf{G}_{hkl}, \tag{1}$$

where $\mathbf{G}_{hkl}$ contains the Miller indices of the diffracting plane, $\mathbf{B}_0$ is a transformation matrix from reciprocal space to the Cartesian grain system of an unstrained grain, ε is the strain tensor, $\mathbf{I}$ is the identity matrix, $\mathbf{g}^{-1}$ is a transformation matrix from the Cartesian grain system to the sample system, $\mathbf{T}$ is a transformation matrix from the sample system to the rotated system, and $\mathbf{\Omega}$ is a transformation matrix from the rotated system to the laboratory system. More specific information on the definitions of these matrices can be found elsewhere (Poulsen, 2004). The diffraction spot for this lattice plane, **Q**, will deviate from the position for a strain-free case, since the diffraction vector describes the direction of the outgoing X-ray (see Fig. 1). The difference between the two positions can then be used for fitting the grain-averaged elastic strain tensor, when enough spots from a single grain are available.

2.1. LabXRS

To enable strain-tensor analysis on a grain scale, the grain structure should be indexed so that the orientations of all relevant grains are known. In practice, this can be carried out using LabDCT or 3DXRD. Given the grain structure, the specific lattice plane (*hkl*) for a spot from a given grain can be assigned using forward simulation [see Fang *et al.* (2020)]. The experimental diffraction vector, $\mathbf{G}_{exp}$, for the given diffraction spot can be determined from the setup geometry, as

$$\mathbf{G}_{exp} = \mathbf{K}_{in} - \mathbf{K}_{out}, \tag{2}$$

where $\mathbf{K}_{in}$ and $\mathbf{K}_{out}$ are the incoming and outgoing wavevectors, respectively (see Fig. 1). These are defined as

$$\mathbf{K}_{in} = \frac{2\pi}{\lambda_{hkl}}\frac{(L_{ss}+x_m, y_m, z_m)}{|(L_{ss}+x_m, y_m, z_m)|} \tag{3}$$

and

$$\mathbf{K}_{out} = \frac{2\pi}{\lambda_{hkl}}\frac{(L_{sd}-x_m,\ y_{det}-y_m,\ z_{det}-z_m)}{|(L_{sd}-x_m,\ y_{det}-y_m,\ z_{det}-z_m)|}, \tag{4}$$

where λ_{hkl} is the wavelength that fulfills the Bragg condition for the particular event; x_m, y_m and z_m are the coordinates of the grain center of mass (**M** in Fig. 1); and y_{det} and z_{det} are the coordinates of the experimental diffraction spot (**Q** in Fig. 1). However, the exact wavelength for a given diffraction event, λ_{hkl}, is difficult to determine due to the use of a polychromatic beam. The lengths of these vectors are therefore unreliable. For this reason, the strain evaluation will be carried out solely on the direction of the diffraction vectors. Once the experimental diffraction vectors are calculated they are transformed to the rotated coordinate system, so that the diffraction vectors from different projections are in the same laboratory coordinate system:

$$\mathbf{G}_{\omega} = \mathbf{\Omega}^{-1}\mathbf{G}_{exp}. \tag{5}$$

The strain tensor can then be analyzed by finding the combination of orientation and strain that minimizes the sum of all angles between the diffraction vectors calculated from the experimentally measured spots, and simulated diffraction vectors for each grain. Since only the angle between the diffraction vectors is considered, the unreliable lengths of the vectors are of no consequence. The minimized function is

$$f(x) = \sum \cos^{-1}\left(\frac{\mathbf{G}_{\omega}}{|\mathbf{G}_{\omega|}} \cdot \frac{\mathbf{TxG}_{hkl}}{|\mathbf{TxG}_{hkl}|}\right). \tag{6}$$

The minimization variable **x** is the product of the orientation matrix $\mathbf{g}^{-1}$ and the reciprocal basis matrix **B**, which contains information on the shape and size of the unit cell, and therefore the strain. The **B** and $\mathbf{g}^{-1}$ matrices are then retrieved

by QR decomposition. The strain tensor is finally calculated using the following equation:

$$\varepsilon = \frac{1}{2}\left[\mathbf{B}_0\mathbf{B}^{-1} + \left(\mathbf{B}_0\mathbf{B}^{-1}\right)^{\top}\right] - \mathbf{I}. \quad (7)$$

For the aforementioned reasons, the fitting is carried out assuming that the dilatational strain is zero, *i.e.* $\varepsilon_{11} + \varepsilon_{22} + \varepsilon_{33} = 0$.

3. Implementation and strain-accuracy analysis

LabXRS, as described above, is validated by using simulated LabDCT data sets, where the ground-truth grain structure (including full orientation data) and strain tensor for each grain are provided as input into a forward-simulation model. Each simulated data set consists of a series of diffraction patterns without any noise. The error of the strain measurement can easily be quantified as the difference between the ground truth and the simulated measurement. In order to examine the effects of both grain position and orientation dependence on the strain accuracy, multiple grains were simulated for each data set. In order to separate the strain tensor from the orientation of each grain, the strain tensors were applied in the Cartesian grain system given for each grain. This means that the strain state of each grain is different macroscopically (in the laboratory system). While this is not a physically realistic situation, it makes quantifying the effects of orientations on the strain accuracy easier. The implementation is outlined in the flow chart shown in Fig. 2.

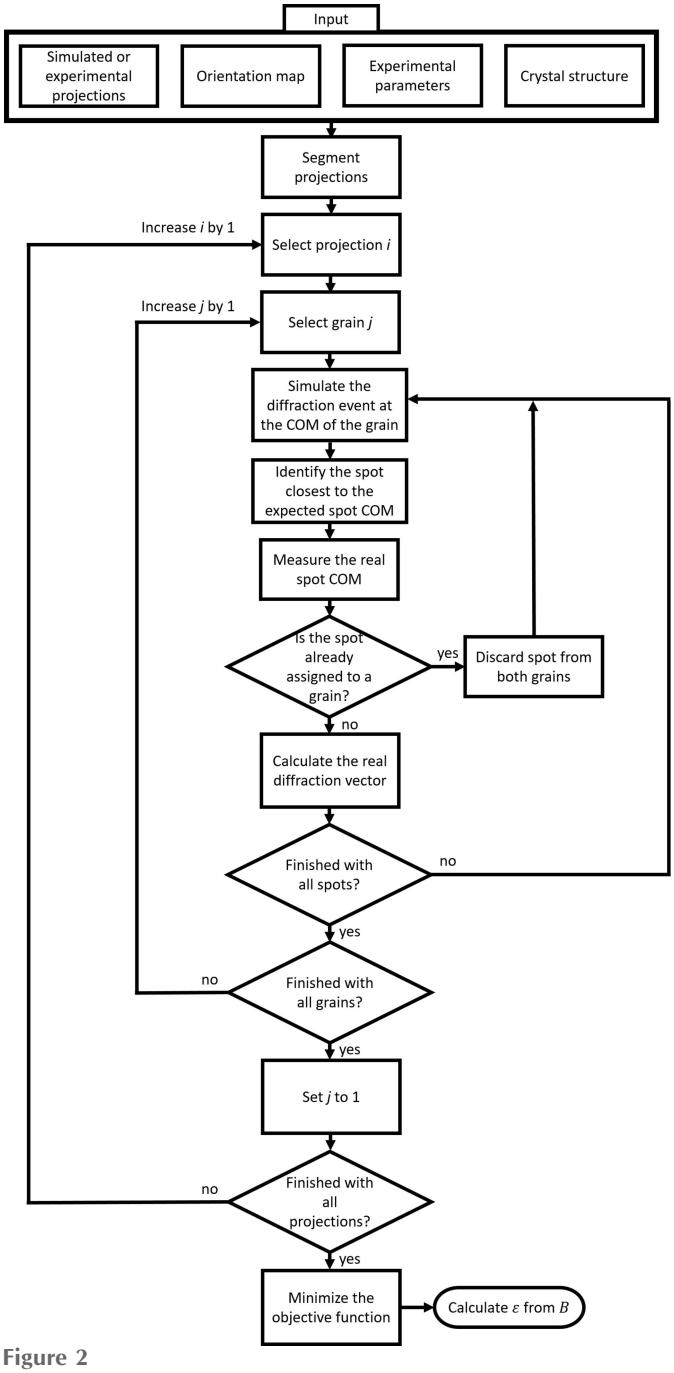

Figure 2
A flow chart of the implementation of LabXRS. COM = center of mass.

3.1. Forward simulation

In order to simulate the strained patterns, the polyhedron-meshing-based forward simulation model developed by Fang *et al.* (2020) was modified to include the strain tensor in the equation calculating the diffraction vectors using equation (1). For the simulation, it is assumed that both the detector and the rotation axis of the sample are perfectly aligned and that no grain has any mosaicity. The grain structure used for the generation is a set of 57 grains with sizes ranging from 30 to 70 µm retrieved from an actual LabDCT data set. These grains were divided into 5–10 polyhedra depending on the individual grain size. These polyhedra were used as the geometry for the forward simulations rather than each individual voxel, to save computation time. A few grains were simulated with twice the number of polyhedra to ensure that the results do not depend on the fineness of this subdivision. The sample is fully recrystallized pure iron (99.95 wt%) with a nearly random texture, and the LabDCT experiment was performed with a Zeiss Xradia 520 Versa. More information on the original data set is available elsewhere (Lindkvist *et al.*, 2021).

Six different sets of setup parameters for the simulated LabDCT experiments were used to examine their effects on the strain resolution (see Table 1). Four different geometrical setups were used. These included a standard LabDCT setup utilizing the Laue focusing effect and a near-field detector (setups 1–3), a magnified setup with a far-field detector (setup 4), a Laue focusing setup with a far-field detector (setup 5), and a near-field setup with a large distance between sample and source (setup 6). It has previously been demonstrated that the magnified geometry increases both the spatial and angular resolution of LabDCT (Fang *et al.*, 2019; Fang, Juul Jensen & Zhang, 2021). For the near-field case (setups 1–3 and 6), the detector was chosen to be an array of 2032 × 2032 pixels with a pixel size of 3.36 × 3.36 µm, identical to the detector in the Zeiss Xradia 520 Versa. For the far-field cases (setups 4 and 5), a detector with a ten times larger pixel size was used in the simulations. Two other parameters were also examined using the near-field Laue focusing geometry, namely the number of projections and pixel binning. The former is an important

Table 1
Experimental setup parameters used for the generation of simulated diffraction patterns.

Setup	L_{ss} (mm)	L_{sd} (mm)	Pixel size (μm)	No. of projections	Detector binning
1	14	14	3.36	121	2
2	14	14	3.36	361	2
3	14	14	3.36	361	1
4	14	200	33.6	361	1
5	200	200	33.6	361	1
6	200	14	3.36	361	1

Table 2
Components of the applied strain tensor for each set of experimental setup parameters.

The strain tensor is symmetric, *i.e.* $\varepsilon_{1,2} = \varepsilon_{2,1}$ *etc*. The strain tensors were applied identically to every grain in the Cartesian grain system.

Data set	$\varepsilon^{app}_{1,1}$	$\varepsilon^{app}_{1,2}$	$\varepsilon^{app}_{1,3}$	$\varepsilon^{app}_{2,2}$	$\varepsilon^{app}_{2,3}$	$\varepsilon^{app}_{3,3}$
A	0	0	0	0	0	0
B	0	10^{-3}	0	0	0	0
C	0	0	10^{-3}	0	0	0
D	0	0	0	0	10^{-3}	0
E	10^{-3}	0	0	-5×10^{-4}	0	-5×10^{-4}

parameter to consider since it is the easiest way to increase the number of spots available for the measurement, solely at the expense of measurement time. The pixel binning is commonly used to sacrifice detector resolution for higher signal-to-noise ratio (SNR) by averaging the intensities of neighboring pixels. Pixel binning of 2 × 2 results into an effective pixel size of 6.72 μm was used for setups 1 and 2.

In order to examine the sensitivity, accuracy and precision of the strain measurement as a function of applied strain tensor, five distinct data sets, each with a unique strain tensor applied to all the grains, were generated for each set of setup parameters (see Table 2). The applied strain tensors were selected to have a realistic magnitude and to test the sensitivity of each shear component along with one example of deviatoric normal strain.

3.2. Noise considerations

For all the setups and applied strain tensors, noise-free diffraction images were used to obtain the theoretical strain accuracy. However, noise is present in experimental images. To examine the effects of noise, two additional types of analysis were included:

First, noise similar to what is observed for relatively poor experimental conditions was applied to the setup 1 projections. Poisson noise was added in a similar fashion to previous work (Fang, Hovad *et al.*, 2021), with a mean background level of 110 and a standard deviation of 13. This is approximately equivalent to the noise levels observed experimentally using setup 1 with an exposure time of 50 s (Lindkvist *et al.*, 2021). The data were then segmented using a simple threshold, treating everything with an intensity above 150 as a potential diffraction spot.

Second, further analysis was made using noise-free data but applying a progressively higher threshold. This simulates the effect where weaker spots are 'drowned' in the noise sooner than brighter spots, as well as outer regions of spots being indistinguishable from the background. This method is analogous to a real experiment as the primary effects governing the intensity of the spots (geometry, exposure time, the X-ray spectrum, quantum detective efficiency) have been taken into account when generating the simulated patterns (Fang *et al.*, 2020). However, the simulations are assuming a near-field detector like the one used in the commercial setup. In reality, a larger detector (as used for setups 4 and 5) may have different properties.

An exposure time of 400 s per projection was chosen to calculate the intensities with each setup.

3.3. Backward strain fitting

LabXRS is implemented in MATLAB. In order to differentiate the spots from the background, the patterns were all segmented with a Laplacian of Gaussian algorithm, resulting in a set of binary images with the spots highlighted (Lind, 2013). The spot center of mass and the corresponding *hkl* indices were determined using forward simulation (Fang *et al.*, 2020). In order to generalize the procedure, the unstrained case was assumed for the forward simulation. A box of 80 × 80 pixels was then defined around each of these coordinates, and the center of mass of the real spot closest to the simulated spot could be determined. This procedure was repeated for each grain and each lattice plane in the first three {*hkl*} families for each rotation step. If only part of a spot was visible on the detector, it was discarded. If the same spot was identified for two different grains (*e.g.* in the case of spots overlapping), it was not assigned to either grain. The primary reason for this is to reduce the potential effects of spot overlap.

Once all the center-of-mass coordinates had been measured for every grain, the diffraction vectors were calculated using equation (3). The objective function, equation (6), was then minimized for each grain using the MATLAB function `fmincon`. An assumption of zero dilatational strain was imposed as a constraint for the fitting procedure, *i.e.* $\varepsilon_{11} + \varepsilon_{22} + \varepsilon_{33} = 0$. The strain tensor for each grain was finally calculated using equation (7).

The minimization problem was solved using a set of different algorithms, including an interior-point algorithm, two sequential quadratic programming algorithms, an active set algorithm and a trust-region algorithm. None of the different algorithms produced meaningfully different results. Therefore, only the results obtained using the interior-point algorithm are presented in this work.

In order to determine the effects of the initial condition (zero-strain assumption), random values were added to the $\mathbf{B}_0$ matrix and the minimization was performed repeatedly with different initial conditions. Random values of the same order of magnitude as the zero-strain $\mathbf{B}_0$ matrix resulted in variations in the resulting strain tensors of the order of 10^{-8}. This does suggest that there is an effect of the initial condition on

the final result as the algorithm does not necessarily always find the global minimum. However, considering the magnitude of the error it does not seem to be much of a concern.

4. Results

Typical projections from the different geometrical setups and the same applied strain tensor, C, for noise-free cases can be seen in Fig. 3. The geometries utilizing the Laue focusing effect produced significantly smaller spots than the magnifying geometry (setup 4). The increased detector pixel size and L_{ss} for setup 5 results in especially small spots, taking up only a few pixels.

Strain tensors for all 57 grains were calculated using the developed algorithm and analyzed with respect to the geometrical setup parameters and applied strain tensors, as well as imaging noise and microstructural parameters, including grain position, size and orientation.

4.1. Effect of geometrical setup parameters and applied strain tensors

In order to show the variation of the measured strain between different grains within the same data set, individual strain components for all grains in data sets C1 and C5 are plotted in the histograms in Figs. 4 and 5, respectively. Since the same strain tensor was applied to each grain, the distribution is strictly due to inaccuracies in the measurement and not to variations from grain to grain.

While both data sets contain outliers, most notably in strain component $\varepsilon_{3,3}$, the general trend suggests errors of the order of magnitude of 10^{-4}. A similar pattern is seen for all other applied strain tensors for each experimental setup. This appears to show that neither the accuracy nor the precision is significantly affected by the applied strain.

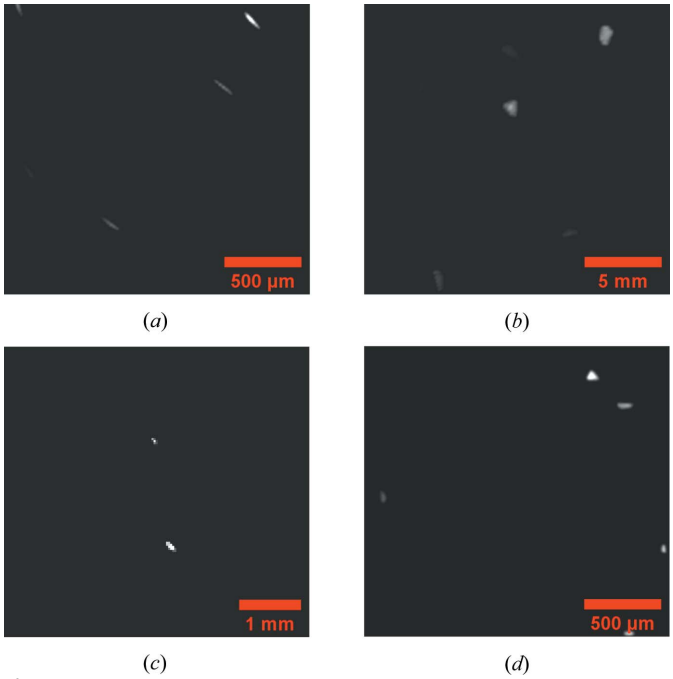

Figure 3
Lower-left portions of typical projections from setups 3, 4, 5 and 6 in (*a*)–(*d*), respectively. The detector size and thus the scale differ between (*a*) and (*b*), and the portion of the projection is smaller in (*c*) to better show the spots, which also changes the scale.

Table 3
The mean difference between measured strain and applied strain as well as the standard deviation, averaged over all 57 grains, the five different strain-tensor inputs and the six strain components.

Setup	Mean($\lvert\varepsilon - \varepsilon^{app}\rvert \times 10^4$)	$\sigma_\varepsilon \times 10^4$
1	0.5	5.1
2	0.4	4.3
3	0.6	4.4
4	0.3	4.0
5	0.1	1.0
6	0.3	2.3

To compare the strain data between different setups, the error is defined as the average difference from the applied strain tensor,

$$\text{mean}(|\varepsilon - \varepsilon^{app}|). \quad (8)$$

This is applied first to all five applied strain tensors, followed by all of the grains, yielding a single error tensor for each setup. The components of the error tensors were then averaged over the six strain components to yield a single error value, which is an accuracy indicator. The errors obtained with this definition, along with the standard deviation for the different experimental setups, can be seen in Table 3. The resulting strain resolution, as indicated by the standard deviation, is in the range of 1–5 $\times 10^{-4}$, with setup 5 being the most precise.

4.2. Effects of microstructural parameters

From Figs. 4 and 5, it is clear that there is a significant variation of the error from grain to grain, despite the idealized case using simulated data and the similar number of spots available for strain fitting. In order to examine the reason for this behavior, correlations between a few geometrical variables and the strain error were examined. Here, the error is defined in a manner similar to what was done previously, but since the error on a grain-by-grain basis is now considered, the strain tensors are not averaged across all grains and applied strain tensors.

Although the comparison was carried out for each data set, only those with applied strain tensor C will be shown here. The errors were normalized by dividing each error by the largest error within the data set. This normalization is used to highlight the influence of individual microstructural parameters while not visualizing the effects of the differences between setups. The latter is more appropriately displayed by the standard deviations in Table 3.

The first variable examined was the grain position within the sample. It was found that the distances along **x**, **y** and **z** have similar effects on the strain error individually, so the relevant variable was determined to be the distance to the center of the examined volume, *i.e.* $(x^2 + y^2 + z^2)^{1/2}$. This

distance was then plotted against the normalized strain error (see Fig. 6). While all the grains with the largest errors are relatively far from the center, it is evident that there are also numerous grains with very small errors at relatively large distances. Similar effects have been observed for strain analysis using HEDM (Lim, 2020), as well as for grain reconstruction using LabDCT (Fang, Juul Jensen & Zhang, 2021).

Next, the effects of the grain size were examined (see Fig. 7). There appears to be no strong correlation in the grain size range examined here, although some specific grains have large errors using several different setups.

Finally, the effects of the orientation of the grains were examined. This was carried out by selecting each setup one by one and relating the strain errors of the grains to the position of the grain in pole figures (see Fig. 8) for setup 1. No clear pattern was revealed from this analysis.

4.3. Effects of noise

The LabXRS analysis performed on the data overlaid with Poisson noise resulted in an increased strain standard deviation of only 5×10^{-5}. This low value suggests that noise itself is not significantly contributing to the error, but it may make segmentation more difficult and thereby indirectly affect the result.

The effects of raising the segmentation threshold, corresponding to increasing the background level, on the standard

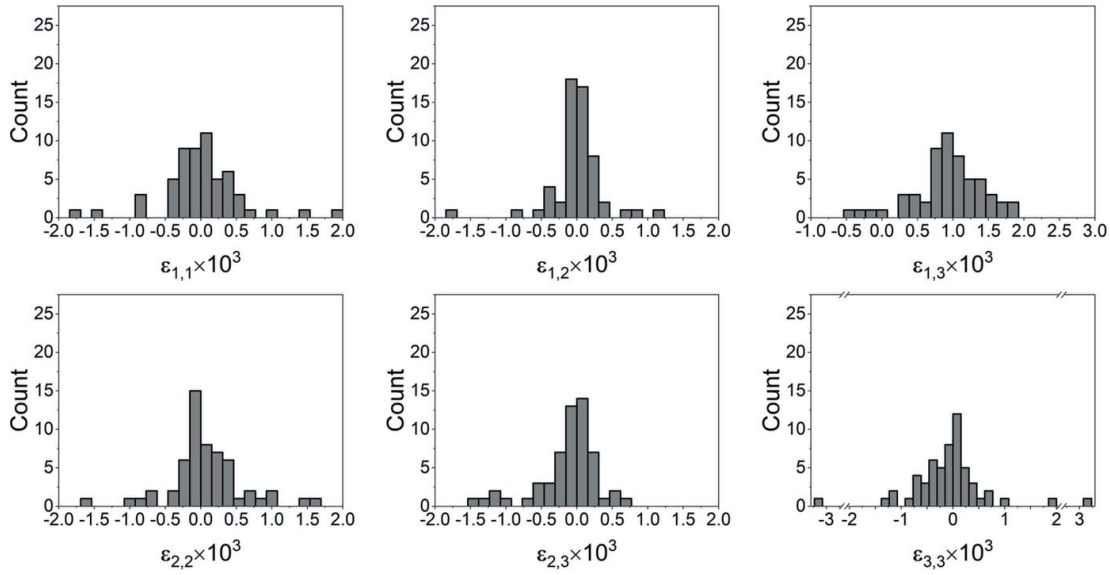

Figure 4
Histograms of each strain component from every grain, measured using setup 1 and with the applied strain of data set C. The *x* axis is shifted for the graph showing the values of $\varepsilon_{1,3}$ due to the applied strain condition.

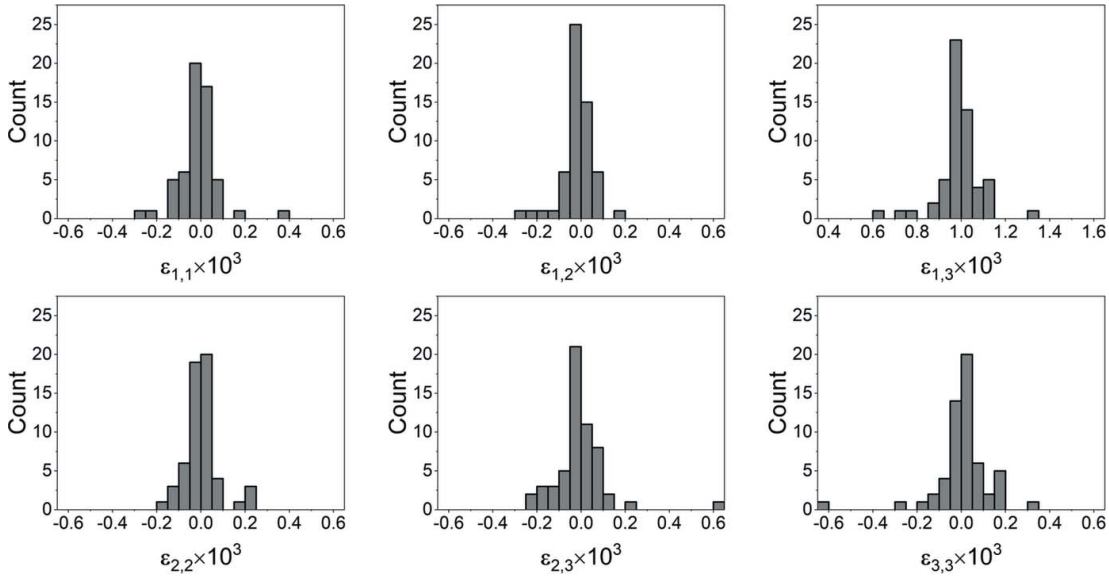

Figure 5
Histograms of each unique strain component from every grain, measured using setup 5 and with the applied strain of data set C. The *x* axis is scaled differently from Fig. 4.

deviation of the strain can be seen in Fig. 9. Setups 1, 2 and 5 are the most robust and are not affected significantly by the increased background level.

The primary effect of increasing the background level is the exclusion of spots of lower intensities. The total number of spots as a function of background level for each setup can be seen in Fig. 10. Setups 1, 2 and 5 retain most of the original spots despite the background increasing and are again found to be the most robust.

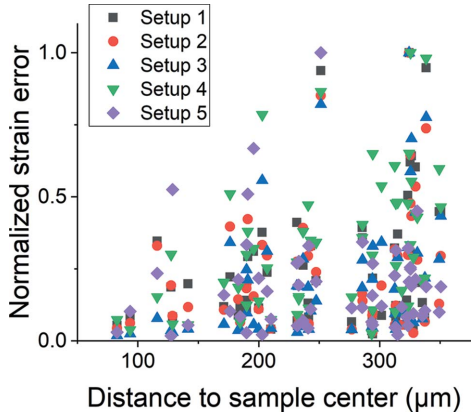

Figure 6
The normalized error of the strain measurement for all grains and all five experimental setups with applied strain tensor C, plotted with respect to the distance from the center of the examined sample volume.

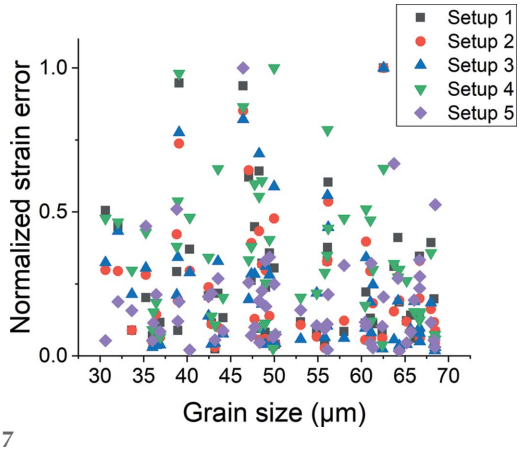

Figure 7
The normalized error of the strain measurement for all grains and all five experimental setups with applied strain tensor C, plotted with respect to the individual grain size.

5. Discussion

The small differences between the applied and measured strain for all setups (see Table 3), suggest that there is no significant bias inherent to the procedure. This shows promise that local 'grain average strain tensor' can be obtained using LabXRS in home laboratories. The results have shown that, similarly to the situation for the synchrotron methods, the sample-to-detector distance is critical for the strain resolution (determined as the standard deviation of the strain errors). The best strain accuracies for the near-field and far-field modes are found to be $\sim 5 \times 10^{-4}$ and $\sim 1 \times 10^{-4}$, respectively, which are very similar to those that can be obtained by the corresponding synchrotron methods (Oddershede *et al.*, 2010; Reischig *et al.*, 2013; Reischig & Ludwig, 2020). However, these numbers are for the idealized cases presented here, and actual experimental results are likely to be worse.

The error also seems to be connected to a number of other variables. The reasons for these behaviors, as well as other effects that will potentially affect experimental results, will be discussed here.

5.1. Effects of sample-to-detector distance

The results show only a very minor decrease in the standard deviation when comparing setups 1–3 with 4. The fact that the resolution is higher when distances between the sample and the detector are increased is well documented for 3DXRD and similar techniques, where the term 'far field' usually refers to experiments with detectors placed further away to provide higher angular resolution. It is expected that this would be the case for LabXRS as well. However, the increased sample-to-detector distance comes with several drawbacks. The one that is likely to explain the relatively slight improvement in accuracy is the geometrical magnification. The magnified spots occupy a larger number of pixels, which increases the error in the center-of-mass determination (see Section 5.2).

There are also some considerations to take into account when implementing far-field setups experimentally. Firstly, commercial LabDCT setups are currently equipped with relatively small detectors, which severely limits the number of

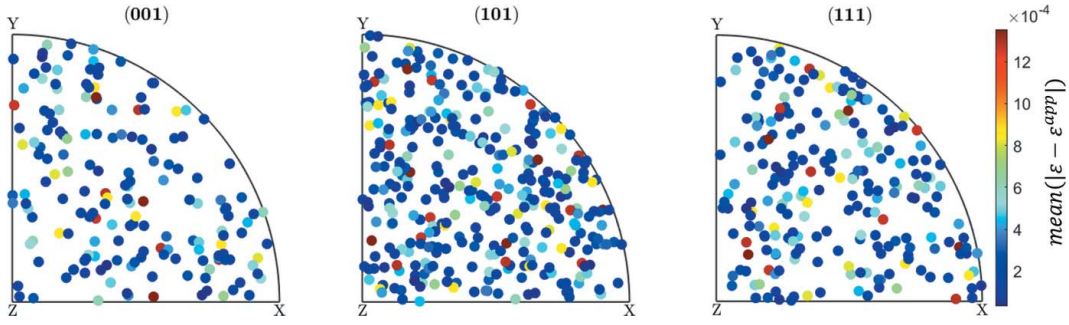

Figure 8
Pole figures with the orientation of each grain marked. The color of the points in each figure relates to the strain error of the individual grain in data set 1C.

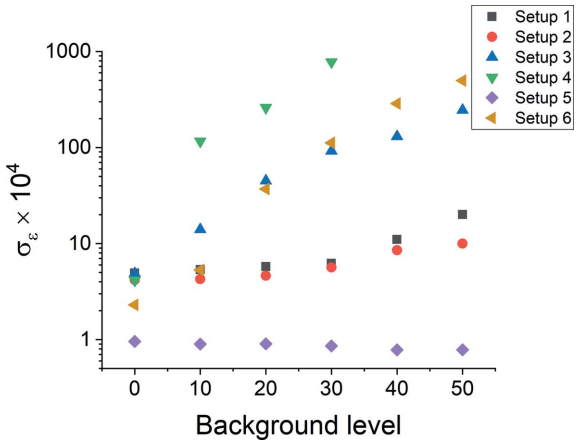

Figure 9
The standard deviation of the strain as a function of the background level added to the data. Two data points from setup 4 are excluded, as the number of spots are drastically reduced, thus leading to convergence issues for the minimization problem.

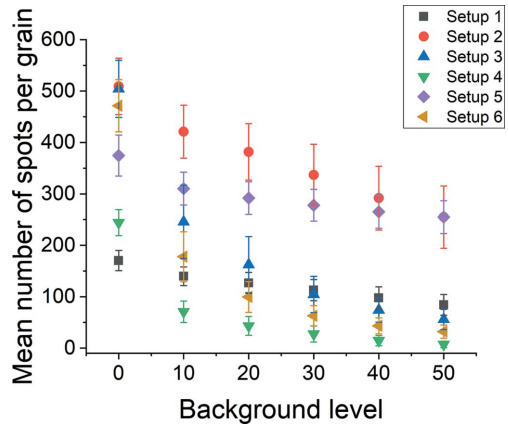

Figure 10
The average number of spots per grain for the strain analysis as a function of the background noise level.

spots that can be collected using distances as large as discussed here. However, since large detectors have already been developed for other applications, this is not a significant obstacle to overcome. A more severe concern regards the SNR. A larger sample-to-detector distance will decrease the amount of diffracted X-ray radiation reaching the detector due to increased interaction with air; this is expected to cause a 5–20% reduction in spot intensity depending on the wavelength of the diffracted X-rays. Therefore, a longer exposure time may be required to increase the SNR. However, larger pixel sizes may provide a higher contrast between spots and background due to the intensity of the spot being integrated over a lower number of pixels, which would ease segmentation without the need to increase the exposure time.

5.2. Effects of source-to-sample distance

The parameter with the seemingly largest positive impact on the strain resolution of LabXRS discussed here is the source-to-sample distance. Additionally, the benefit of extending L_{sd} is increased when proportionally extending L_{ss}.

Whereas the increased angular resolution as a function of increasing L_{sd} in similar synchrotron techniques (utilizing monochromatic X-rays) is clear, the reason for the significantly improved resolution when increasing L_{ss} in the laboratory setup is less obvious. It is, however, mainly related to the use of a conical polychromatic X-ray source in the laboratory. The strain determination is based on evaluation of the diffraction vector, which is calculated from both the incoming and outgoing wavevectors of the diffraction event taking place at the center of mass of the grain. This outgoing wavevector is assumed to point towards the center of mass of the diffraction spot, as measured by the detector and using the pixel intensity as a weight. However, with a polychromatic beam this assumption is not completely correct. The primary reason is that the intensity of the different parts of the spot varies depending not only on the volume of the grain (as it does for a monochromatic beam) but also on the energy of the diffracting X-rays. With conical polychromatic X-rays, different parts of the grains diffract X-rays with different energies. The intensities recorded on the detector will generally be lower for X-rays of higher energies as both the X-ray spectrum of the source and the detective quantum efficiency are lower for the higher energies. As L_{ss} increases, the energies diffracting from each grain for each rotation fall within a narrower band (*i.e.* become more monochromatic), because the angles between each incoming wavevector of the different parts of the grain shrink. As a result, the shifts in the center of mass of a spot caused by the X-ray energy variations become smaller; hence the strain accuracy increases. A similar geometrical argument could explain the comparatively poor strain accuracy for magnified setups (*e.g.* setup 4), where further spot-intensity variation is caused by the fact that different parts of the grain are magnified slightly differently.

A drawback of increasing the source-to-sample distance may be a significant decrease in SNR. This is because of the conical beam requiring a smaller aperture in order to limit the beam to the sample, therefore drastically decreasing the flux in proportion to the increased distance. What this means for the data is that the spots may be more difficult to differentiate from the background on the detector, necessitating the use of longer exposure times. However, the SNR only scales with the square root of the exposure time (Strum & Fenigstein, 2014) and there are inherent limitations on how long a time can be used. Nevertheless, the Laue focusing effect and the large detector pixel size used (*e.g.* from setup 5) may counterbalance this issue. Also it may become less of a concern as more efficient segmentation techniques are developed, *e.g.* techniques utilizing deep-learning algorithms that have recently been proven to be effective for removing background noise (Fang, Hovad *et al.*, 2021).

5.3. Effects of binning and the number of projections

From Table 3 it is suggested that the effect of binning on the strain resolution is negligible, as the standard deviation of the

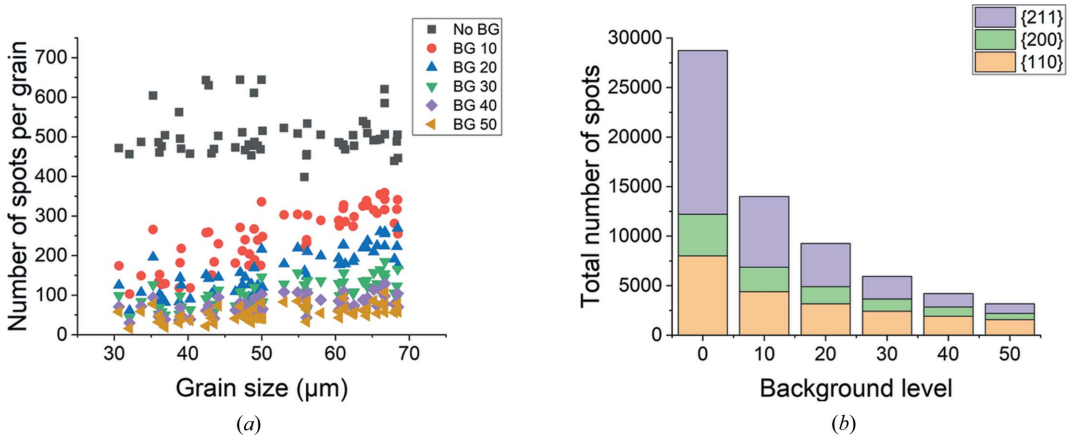

Figure 11
Graphs showing the bias towards filtering away spots from smaller size (*a*) and spots from higher-order {*hkl*} (*b*) due to an increase in background noise level in setup 3. BG = background.

strain is only slightly lower with binning than without. This may be a surprising result since binning effectively reduces the resolution of the detector. However, since the algorithm uses the center of mass of the spots, a sub-pixel resolution is achieved regardless. This is a promising result for practical experiments since binning is a useful tool to increase the SNR. The number of projections is expected to increase the strain resolution, as more projections result in more available spots and therefore more data to average out inaccuracies. The effects of this can also be seen in the data, although the relatively minor benefit of adding more projections may not be worth the additional time for the experiment beyond a certain point. This is also consistent with previous research showing that the angular resolution of the indexing is not very significantly increased by increasing the number of projections from *e.g.* 41 to 121 (Lindkvist *et al.*, 2021).

5.4. Effects of noise

The investigation of effects of simulated noise (in Section 4.3) reveals almost no effect on the precision of the strain measurement when adding Poisson noise. This is clear as the method relies only on the center of mass of the spots, which is unlikely to shift significantly due to noise. The possible small shifts are furthermore averaged out in most cases, since multiple spots are used in the strain determination.

Concerning effects of the background noise level, the results suggest that setup 5 is the most robust. The primary reason for this is the high degree of focusing, causing the entirety of the spots to only occupy a few pixels and resulting in high spot intensity despite the lower flux (caused by the high L_{ss}). Setups 4 and 6 are found to be the least robust. In these cases, the spots are magnified and comparatively weak. Even at relatively low background levels, many spots are filtered away (see Fig. 10).

Pixel binning is advantageous when the noise level is high. This is clear when comparing setups 2 and 3 (see Fig. 9). With binning, the spots are brighter and are consequently not filtered away as readily as when pixel binning is not used. When noise is considered, more projections are also beneficial, especially when the background level is high (see setups 1 and 2 in Fig. 9). This is simply because more projections result in more spots.

However, the total number of spots is not the only determining factor. For example, setups 1 and 3 have approximately the same number of spots when all intensities below 30 are filtered away (see Fig. 10), but the standard deviation in strain is one order of magnitude higher for setup 3 (see Fig. 9). The main reason for this is that the filtering away of spots is not random (see Fig. 11). Spots have different intensities depending on both the size of the diffracting grain and the Miller indices of the diffracting plane. For setup 3, smaller grains tend to produce weaker spots, simply due to fewer X-rays interacting with the grain, so they are filtered out sooner [see Fig. 11(*a*)]. Higher-order {*hkl*} produce weaker spots, which are also filtered out sooner [see Fig. 11(*b*)]. There are two reasons for this: (i) the structure factor for higher-order {*hkl*} is smaller; and (ii) the X-rays diffracted by higher-order {*hkl*} generally have higher energies, and both the X-ray spectrum and detective quantum efficiency of the detector are lower for higher-energy X-rays. Fewer higher-order {*hkl*} spots leads to less diversity of linearly independent diffraction vectors, and thus poor strain resolution.

6. Conclusions and outlook

A new procedure, LabXRS, to map strains on a grain scale in three dimensions non-destructively using LabDCT data has been presented and validated using simulated data. The effects of various experimental and microstructural parameters on the strain resolution have been examined. The following conclusions can be drawn:

(1) Grain-scale strain tensors can be analyzed in home laboratories using LabDCT data. The best theoretical strain resolution observed using this technique was 1×10^{-4} in the present analysis, which is sufficient to characterize both the local strain responses to an applied load and residual strains on a grain scale for most engineering materials.

(2) The distances between the source and sample and between the sample and detector are both important for the strain resolution; large distances (of the order of 100 mm) are needed to improve the strain resolution. Laue focusing geometry is preferred compared with magnified geometry, to increase the SNR and to limit the heterogeneous spot-intensity spread caused by different X-ray wavelengths.

(3) The effects of pixel binning did not have a significant effect on the strain accuracy in a noise-free environment. This is mainly because the analysis method only uses the center of mass of the spot, enabling sub-pixel accuracy. It is, however, suggested to employ pixel binning for real experiments to increase the SNR.

(4) More spots added by increasing the number of projections above a certain value do not provide any substantial improvement, while more spots from different (*hkl*) planes are beneficial.

(5) The grain position within the sample influences the strain accuracy, while the effects of orientation on the strain resolution are minor. Experimentally, the strain accuracy for small grains can be relatively poor compared with that for large grains, as there are more spots available from more {*hkl*} families for the larger ones.

The present study provides valuable guidelines for implementing this new functionality experimentally. Also, the strain-mapping procedure will be useful for improving current indexing algorithms by incorporating strain into the indexing procedure.

Acknowledgements

The authors thank Professor Dorte Juul Jensen for invaluable discussions.

Funding information

The following funding is acknowledged: Danmarks Frie Forskningsfond (grant No. 8022-00340B).

References

Bachmann, F., Bale, H., Gueninchault, N., Holzner, C. & Lauridsen, E. M. (2019). *J. Appl. Cryst.* **52**, 643–651.
Bernier, J. V., Barton, N. R., Lienert, U. & Miller, M. P. (2011). *J. Strain Anal. Eng. Des.* **46**, 527–547.
Bhattacharyya, J. J., Nair, S., Pagan, D. C., Tari, V., Rollett, A. D. & Agnew, S. R. (2020). *Acta Mater.* **197**, 300–308.
Chung, J.-S. & Ice, G. E. (1999). *J. Appl. Phys.* **86**, 5249–5255.
Fang, H., Hovad, E., Zhang, Y., Clemmensen, L. K. H., Ersbøll, B. K. & Juul Jensen, D. (2021). *IUCrJ*, **8**, 719–731.
Fang, H., Juul Jensen, D. & Zhang, Y. (2019). *IOP Conf. Ser. Mater. Sci. Eng.* **580**, 012030.
Fang, H., Juul Jensen, D. & Zhang, Y. (2020). *Acta Cryst.* A**76**, 652–663.
Fang, H., Juul Jensen, D. & Zhang, Y. (2021). *IUCrJ*, **8**, 559–573.
Hall, S. A., Hurley, R. C. & Wright, J. (2018). *Micro to MACRO Mathematical Modelling in Soil Mechanics. Trends in Mathematics.* pp. 169–176. Cham: Birkhäuser.
Hayashi, Y., Hirose, Y. & Seno, Y. (2015). *J. Appl. Cryst.* **48**, 1094–1101.
Jakobsen, B., Poulsen, H. F., Lienert, U., Almer, J., Shastri, S. D., Sørensen, H. O., Gundlach, C. & Pantleon, W. (2006). *Science*, **312**, 889–892.
Jensen, D. J. & Poulsen, H. F. (2012). *Mater. Charact.* **72**, 1–7.
King, A., Reischig, P., Adrien, J. & Ludwig, W. (2013). *J. Appl. Cryst.* **46**, 1734–1740.
King, A., Reischig, P., Adrien, J., Peetermans, S. & Ludwig, W. (2014). *Mater. Charact.* **97**, 1–10.
Larson, B. C. & Levine, L. E. (2013). *J. Appl. Cryst.* **46**, 153–164.
Larson, B. C., Yang, W., Ice, G. E., Budai, J. D. & Tischler, J. Z. (2002). *Nature*, **415**, 887–890.
Levine, L. E., Geantil, P., Larson, B. C., Tischler, J. Z., Kassner, M. E., Liu, W., Stoudt, M. R. & Tavazza, F. (2011). *Acta Mater.* **59**, 5803–5811.
Lim, R. E. (2020). PhD thesis, Carnegie Mellon University, Pittsburgh, Pennsylvania, USA.
Lind, J. F. (2013). PhD thesis, Carnegie Mellon University, Pittsburgh, Pennsylvania, USA.
Lindkvist, A., Fang, H., Juul Jensen, D. & Zhang, Y. (2021). *J. Appl. Cryst.* **54**, 99–110.
Ludwig, W., Schmidt, S., Lauridsen, E. M. & Poulsen, H. F. (2008). *J. Appl. Cryst.* **41**, 302–309.
Margulies, L., Winther, G. & Poulsen, H. F. (2001). *Science*, **291**, 2392–2394.
McDonald, S. A., Burnett, S. L., Donoghue, J., Gueninchault, N., Bale, H., Holzner, C., Lauridsen, E. M. & Withers, P. J. (2021). *Mater. Charact.* **172**, 110814.
McDonald, S. A., Holzner, C., Lauridsen, E. M., Reischig, P., Merkle, A. P. & Withers, P. J. (2017). *Sci. Rep.* **7**, 5251.
McDonald, S. A., Reischig, P., Holzner, C., Lauridsen, E. M., Withers, P. J., Merkle, A. P. & Feser, M. (2015). *Sci. Rep.* **5**, 14665.
Menasche, D. B., Shade, P. A. & Suter, R. M. (2020). *J. Appl. Cryst.* **53**, 107–116.
Miller, M. P., Pagan, D. C., Beaudoin, A. J., Nygren, K. E. & Shadle, D. J. (2020). *Metall. Mater. Trans. A*, **51**, 4360–4376.
Oddershede, J., Schmidt, S., Poulsen, H. F., Margulies, L., Wright, J., Moscicki, M., Reimers, W. & Winther, G. (2011). *Mater. Charact.* **62**, 651–660.
Oddershede, J., Schmidt, S., Poulsen, H. F., Sørensen, H. O., Wright, J. & Reimers, W. (2010). *J. Appl. Cryst.* **43**, 539–549.
Oddershede, J., Sun, J., Gueninchault, N., Bachmann, F., Bale, H., Holzner, C. & Lauridsen, E. (2019). *Integr. Mater. Manuf. Innov.* **8**, 217–225.
Poulsen, H. F. (2004). *Three-Dimensional X-ray Diffraction Microscopy*. Heidelberg: Springer.
Poulsen, H. F., Cook, P. K., Leemreize, H., Pedersen, A. F., Yildirim, C., Kutsal, M., Jakobsen, A. C., Trujillo, J. X., Ormstrup, J. & Detlefs, C. (2018). *J. Appl. Cryst.* **51**, 1428–1436.
Poulsen, H. F., Nielsen, S. F., Lauridsen, E. M., Schmidt, S., Suter, R. M., Lienert, U., Margulies, L., Lorentzen, T. & Juul Jensen, D. (2001). *J. Appl. Cryst.* **34**, 751–756.
Reischig, P., King, A., Nervo, L., Viganó, N., Guilhem, Y., Palenstijn, W. J., Batenburg, K. J., Preuss, M. & Ludwig, W. (2013). *J. Appl. Cryst.* **46**, 297–311.
Reischig, P. & Ludwig, W. (2020). *Curr. Opin. Solid State Mater. Sci.* **24**, 100851.
Simons, H., Haugen, A. B., Jakobsen, A. C., Schmidt, S., Stöhr, F., Majkut, M., Detlefs, C., Daniels, J. E., Damjanovic, D. & Poulsen, H. F. (2018). *Nat. Mater.* **17**, 814–819.
Simons, H., King, A., Ludwig, W., Detlefs, C., Pantleon, W., Schmidt, S., Stöhr, F., Snigireva, I., Snigirev, A. & Poulsen, H. F. (2015). *Nat. Commun.* **6**, 6098.
Strum, A. & Fenigstein, A. (2014). *High Performance Silicon Imaging: Fundamentals and Applications of CMOS and CCD Sensors*. pp. 348–372. Sawston: Woodhead Publishing.
Sun, J., Lyckegaard, A., Zhang, Y. B., Catherine, S. A., Patterson, B. R., Bachmann, F., Gueninchault, N., Bale, H., Holzner, C.,

Lauridsen, E. & Juul Jensen, D. (2017). *IOP Conf. Ser. Mater. Sci. Eng.* **219**, 012039.
Sun, J., Zhang, Y., Lyckegaard, A., Bachmann, F., Lauridsen, E. M. & Juul Jensen, D. (2019). *Scr. Mater.* **163**, 77–81.
Zhang, Y., Andriollo, T., Faester, S., Barabash, R., Xu, R., Tiedje, N., Thorborg, J., Hattel, J., Juul Jensen, D. & Hansen, N. (2019). *Acta Mater.* **167**, 221–230.
Zhang, Y. & Barabash, R. (2019). *QuBS*, **3**, 6.